X-valley leakage in GaAs-based midinfrared quantum cascade lasers: A Monte Carlo study

X. Gao, D. Botez, and I. Knezevic[a)]
Department of Electrical and Computer Engineering, University of Wisconsin–Madison, 1415 Engineering Drive, Madison, Wisconsin 53706-1691

(Received 8 December 2006; accepted 15 January 2007; published online 16 March 2007)

We present a detailed Monte Carlo simulation of electron transport incorporating both Γ- and *X*-valley states in GaAs-based quantum cascade lasers (QCLs). Γ states are calculated using the $\mathbf{K}\cdot\mathbf{p}$ method, while *X* states are obtained within the effective mass framework. All the relevant electron-phonon, electron-electron, and intervalley scattering mechanisms are included. We investigate the *X*-valley leakage in two equivalent-design GaAs/AlGaAs QCLs with 33% and 45% Al-barrier compositions. We find that the dominant *X*-valley leakage path in both laser structures is through interstage $X\rightarrow X$ intervalley scattering, leading to a parallel leakage current J_X. The magnitude of J_X depends on the temperature and occupation of the *X* subbands, which are populated primarily by the same-stage scattering from the Γ-continuum (Γ_c) states. At 77 K, J_X is small up to very high fields in both QCLs. However, at room temperature the 33% QCL shows a much higher J_X than the 45% QCL even at low fields. The reason is that in the 33% QCL the coupling between the Γ-localized (Γ_l) states and the next-stage Γ_c states is strong, which facilitates subsequent filling of the *X* states through efficient intrastage $\Gamma_c\rightarrow X$ scattering; with high *X*-valley population and high temperature, efficient interstage $X\rightarrow X$ scattering yields a large J_X. In contrast, good localization of the Γ_l states in the 45% QCL ultimately leads to low *X*-valley leakage current up to high fields. Very good agreement with experiment is obtained at both cryogenic and room temperatures. © *2007 American Institute of Physics*. [DOI: 10.1063/1.2711153]

I. INTRODUCTION

Midinfrared (mid-IR) GaAs-based quantum cascade lasers (QCLs) have so far utilized Al content of 33%,[1–3] 45%,[4–9] and 100% (Refs. 10–12) in the AlGaAs barrier layers. The first GaAs QCL structure[1] employed 33% Al in the barriers, and emitted at $\lambda=9.4$ μm under pulse operation up to 140 K. With a low-loss Al-free waveguide,[2] the threshold-current density J_{th} of 2–mm-long, 33% Al QCLs was reduced to an average of 5.0 kA/cm^2 at 77 K, and a maximum pulsed operation temperature of 200 K. Mid-IR GaAs QCLs with 33% Al in the barriers have so far achieved a maximum operating temperature of 285 K under pulsed operation,[3] but have not achieved continuous wave (cw) operation.

However, remarkable progress has been made in the device performance of GaAs/$Al_{0.45}Ga_{0.55}As$ QCLs, since their first realization.[4] Room-temperature pulsed operation has been reported for several active region designs, i.e., three quantum-well active regions emitting at 9.0 μm,[4,5] a superlattice active region emitting at 12.6 μm,[6] and a bound-to-continuum design emitting at 11.0 μm.[7] cw operation of 45% Al QCLs based on the original design[4] has been recently achieved[8,9] through optimized device processing, with a T_{max} of 150 K.[9]

Although mid-IR GaAs QCLs have achieved dramatic progress, these devices show a rather poor performance compared to InP-based mid-IR QCLs, which can lase in the cw regime at room temperature.[13–15] The relatively high-threshold-current density and power consumption[16] of GaAs-based QCLs have made it very challenging to achieve room-temperature cw operation.

To further improve the performance of GaAs/AlGaAs QCLs, a detailed knowledge of possible current leakage paths and carrier loss in particular designs is highly desirable. The 45% Al QCL structure[4] showed much better temperature dependence of J_{th} than the 33% Al QCL design,[2] which is believed to be predominantly due to the suppression of the leakage arising from the scattering of carriers from the injector states to the Γ-valley continuum states.[16,17] On the other hand, intervalley scattering is possible at high fields and high temperatures, and might limit the high-field (high-current) operation of a QCL design.[18] With further increase of the barrier Al content, once the upper lasing level becomes aligned with the lowest *X*-valley state of the injection barrier, lasing is suppressed due to intervalley carrier transfer, which limits the emission wavelengths to above 8 μm.[12] Although the leakage via the Γ-continuum states has been well recognized[4,16,17] and studied theoretically,[19] satellite-valley leakage has not been systematically investigated in theory. A systematic theoretical modeling of both Γ- and *X*-valley transport in GaAs/AlGaAs QCL structures is an essential step toward improvement of existing designs.

Much theoretical work has been done, accompanying the rapid experimental developments of QCLs. These include Monte Carlo simulation,[20–23] self-consistent rate equations model,[19,24] as well as nonequilibrium Green's function (NEGF) formalism,[25,26] none of which has accounted for satellite-valley leakage. Whether the nature of charge trans-

[a)]Electronic mail: knezevic@engr.wisc.edu

port in QCL structures is incoherent or coherent is a long-term issue of debate. Theoretical studies by Iotti *et al.*[20,21] showed that although clear coherent oscillations and gain overshoot were observed during the initial transient, the oscillations are damped on a subpicosecond timescale, much shorter than the average transit time across one period. These features have been observed experimentally[27,28] and the timescales are comparable, leading to a conclusion that the resulting steady-state transport in QCLs is semiclassical (incoherent) in nature. Considering the enormous computational burden of the NEGF method, and the fact that semiclassical simulations[19–24] have so far provided very reliable data and insights, in this work, incoherent stationary transport in mid-IR GaAs QCLs is assumed and a Monte Carlo approach is employed.

In this article, we extend the Monte Carlo model[20] of QCL structures to incorporate both Γ- and *X*-valley transport. Our model[29] solves for Γ states utilizing the $\mathbf{K}\cdot\mathbf{p}$ method within the envelope-function approximation, and for *X* states within the effective mass framework. All the relevant interaction mechanisms are included, i.e., electron-longitudinal polar optical (electron-LO) phonon, electron-electron, and intervalley scattering processes within the same stage and between adjacent stages. We apply this model to simulate two GaAs-based mid-IR QCLs with equivalent designs: the 33% Al QCL of Refs. 1 and 2, and the 45% Al QCL of Ref. 4. Designs of these two QCLs are equivalent,[4] since they have similar emitting wavelengths (~9 μm), threshold fields (48 kV/cm), dipole matrix elements (1.6 nm for the 33% QCL, and 1.7 nm for the 45% QCL), and lifetimes in the upper lasing level (1.5 and 1.4 ps, respectively). The dominant *X*-valley leakage path in both QCLs is found to be through interstage $X \rightarrow X$ intervalley scattering. The *X*-valley states are populated predominantly by efficient same-stage scattering from the Γ-continuum states (Γ_c for brevity). The 33% QCL shows a very high *X*-valley leakage current at room temperature even at low fields. The calculated J_{th} values agree well with experiment for both QCLs.

The remainder of this article is organized as follows. In Sec. II, we first review the Monte Carlo transport model for QCL structures, and then present the details of the Γ- and *X*-valley electronic states calculation (Sec. II A), used to compute all the relevant scattering rates (Secs. II B 1, II B 2, and II B 3). In Sec. III, we first illustrate the Γ- and *X*-subband wave functions, and then analyze the field versus current density characteristics at different temperatures, together with the field dependence of the Γ- and *X*-valley electron occupation; we show how the *X*-valley leakage current occurs, and how it affects the performance of different QCL structures. Finally, we conclude with a brief summary in Sec. IV.

II. THEORETICAL APPROACH

Mid-IR QCL heterostructures are usually grown along the *z* axis (001), with the *x-y* plane parallel to the layers. Electronic states near the minima of the Γ and *X* valleys are characterized by $|\mathbf{k}\alpha\rangle = |\mathbf{k},\ \nu\lambda\eta\rangle$, where $\mathbf{k}=(k_x,\ k_y)$ is the in-plane wave vector, ν is the subband, λ denotes the stage, and

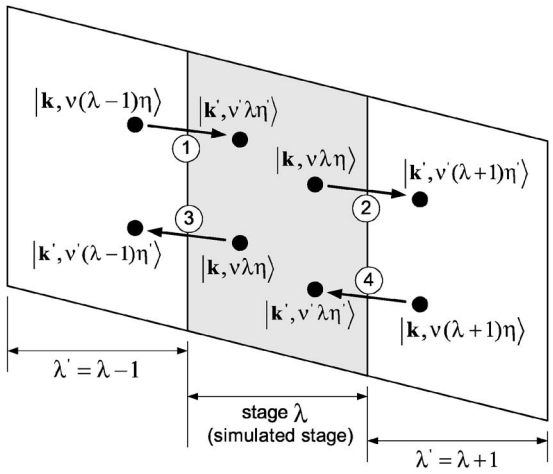

FIG. 1. Schematic of three adjacent stages under an applied field.

η is the valley index ($\eta=\Gamma,\ X_x,\ X_y,\ X_z$). The electron distribution function $f_{\mathbf{k}\alpha}$ evolves with time according to the Boltzmann-like transport equation[20]

$$\frac{d}{dt}f_\alpha(\mathbf{k}) = \sum_{\mathbf{k}'\alpha'} [S^{\alpha}_{\alpha'}(\mathbf{k}',\ \mathbf{k})f_{\alpha'}(\mathbf{k}')(1-f_\alpha(\mathbf{k})) - S^{\alpha'}_{\alpha}(\mathbf{k},\ \mathbf{k}')f_\alpha(\mathbf{k})(1-f_{\alpha'}(\mathbf{k}'))], \quad (1)$$

which can be solved using the ensemble Monte Carlo (EMC) method.[30] $S^{\alpha'}_{\alpha}(\mathbf{k},\ \mathbf{k}')$ is the total transition rate from state $|\mathbf{k}\alpha\rangle$ to $|\mathbf{k}'\alpha'\rangle$, and $S^{\alpha'}_{\alpha}=\Sigma_s\, S^{\alpha'}_{\alpha,\,s}$, with the sum over all possible scattering mechanisms *s*.

The translational symmetry of QCL structures (i.e., the wave functions in any two stages are simple translations in space and energy) allows us to simulate carrier transport over a generic central stage λ only. Spatially remote stages have little wave function overlap with the central stage, making it sufficient to limit the interstage scattering ($\lambda' \neq \lambda$) to the nearest neighbors ($\lambda' = \lambda \pm 1$). Figure 1 shows a schematic of three adjacent stages under bias. In addition, the periodicity of the structures ensures the validity of the charge-conserving scheme[20] employed in the EMC simulation: Each time an electron in a state $|\mathbf{k},\ \nu\lambda\eta\rangle$ undergoes an interstage scattering process to a new state $|\mathbf{k}',\ \nu'(\lambda\pm1)\eta'\rangle$ (e.g., processes 2 and 3 in Fig. 1), another electron is properly injected into the central region by the corresponding processes 1 and 4, so that the number of electrons in the simulated stage λ is conserved. Furthermore, the transition rates for processes 2 and 3 can be regarded the same as those of processes 1 and 4, respectively, thanks to the translational symmetry. As a benefit of this equivalence, we only need to solve for energy levels and wave functions in two full adjacent stages (e.g., stage λ and λ+1) to compute all the intrastage ($\lambda' = \lambda$) and nearest-neighbor interstage ($\lambda' = \lambda \pm 1$) transition rates.

The current density *J* across the whole device is defined in terms of the net electron flux at the interface between the simulated stage λ and the next stage λ+1

$$J \propto \sum_{\mathbf{k}\nu\eta} \sum_{\mathbf{k}'\nu'\eta'} [S^{\nu'(\lambda+1)\eta'}_{\nu\lambda\eta}(\mathbf{k}, \mathbf{k}') f_{\nu\lambda\eta}(\mathbf{k}) - S^{\nu'\lambda\eta'}_{\nu(\lambda+1)\eta}(\mathbf{k}, \mathbf{k}') f_{\nu(\lambda+1)\eta}(\mathbf{k})]. \quad (2)$$

In the EMC implementation, J is attained by counting the interstage scattering events. The details of obtaining the energy levels and wave functions in stages λ and $\lambda+1$ are described in the next section.

A. Electronic states

In most literature on QCL modeling, Γ-valley electronic states are obtained using the conduction-band effective mass equation, whereas we employ the $\mathbf{K}\cdot\mathbf{p}$ method to obtain the Γ states. The $\mathbf{K}\cdot\mathbf{p}$ method provides a good way of solving for the electronic band structure near the band edges, where most of the interesting physical phenomena occur in optical devices. It can conveniently account for the lattice-mismatch strain effect, and the influence of valence bands in narrow-gap semiconductor materials.[31] Although this work focuses on the simulation of GaAs/AlGaAs QCL structures, where the AlGaAs layers are lattice-matched to the GaAs substrate in the whole range of Al contents, the utilization of the $\mathbf{K}\cdot\mathbf{p}$ method makes it straightforward to simulate strain-compensated InP-based QCLs.[32]

The standard eight-band $\mathbf{K}\cdot\mathbf{p}$ model[33,34] consists of the conduction band (c), the heavy-hole (hh) and light-hole (lh), and the spin-orbit split-off (so) band, with their spin degeneracies. The Hamiltonian matrix can be found for unstrained[33] and lattice-mismatched biaxially strained[34] bulk semiconductors without external perturbation. With the in-plane wave vector $\mathbf{k}=0$ and the spin degeneracy accounted for, the eight-band $\mathbf{K}\cdot\mathbf{p}$ model reduces to a three-band model, with the hh band factoring out. We reproduce the three-band $\mathbf{K}\cdot\mathbf{p}$ Hamiltonian matrix elements in the Appendix, with the parameters relevant to our work.

Within the envelope function approximation (EFA) and the three-band $\mathbf{K}\cdot\mathbf{p}$ model, the full Γ-valley carrier wave functions near the zone center in each layer of a heterostructure can be written as[31,33]

$$\Psi^{\Gamma}_{n,\mathbf{k}}(\mathbf{r}, z) = \frac{1}{\sqrt{A}} e^{i\mathbf{k}\cdot\mathbf{r}} \sum_j \psi^{\Gamma}_{n,j}(z) u^{\Gamma}_{j0}(\mathbf{r}, z), \quad (3)$$

where A is the normalization area, $\mathbf{r}=(x, y)$, j sums over the three bands (c, lh, so), and $\psi^{\Gamma}_{n,j}(z)$ is the normalized envelope function, slowly varying with coordinate z over the elementary cells of the lattice; the periodic Bloch function $u^{\Gamma}_{j0}(\mathbf{r}, z)$ conserves its bulk properties within each layer except the small (1–2 monolayer wide) regions in the vicinity of the interfaces, and is assumed not to differ much as we travel from layer to layer. We should note that $|\mathbf{k}| \ll \pi/a$ in Eq. (3), with a being the monolayer width, because we consider electron states near the minimum of the Γ valley.

In the presence of an external potential, the envelope functions $\psi^{\Gamma}_{n,j}(z)$ satisfy the second-order differential equations[31,33]

$$\sum_{j'} [H_{jj'}(\mathbf{k}=0, k_z) + U_{\Gamma}(z)\delta_{jj'}]\psi^{\Gamma}_{n,j'}(z) = E^{\Gamma}_n \psi^{\Gamma}_{n,j}(z), \quad (4)$$

where $H_{jj'}(\mathbf{k}=0, k_z)$ are the elements of the 3×3 $\mathbf{K}\cdot\mathbf{p}$ matrix in Eq. (A1), and k_z will be replaced by the differential operator $-i\partial/\partial z$; $\delta_{jj'}$ is the Kronecker delta, and j' runs over the three bands (c, lh, so); the external perturbation $U_{\Gamma}(z) = -|e|F(z-d/2) - |e|\phi(z)$, where F is the applied uniform electric field, and $\phi(z)$ is the electrostatic potential owing to the specific distribution of free electrons from dopants in the system. $\phi(z)$ is disregarded in our simulation, since its effect on the electronic states is negligible[24] for doping levels below 4.0×10^{11} cm^{-2}. The band discontinuity at the interfaces is taken into account in E_c and E_v in the $H_{jj'}$ matrix.

The coupled differential Eqs. (4) may be solved using the transfer matrix method,[35] the finite difference method,[36] or the finite element method.[37] However, since all these real-space numerical methods would generate spurious solutions [i.e., solutions outside of the first Brillouin zone (BZ)],[38] extra care is needed to select the proper eigenenergies.[34] The reciprocal-space numerical technique[39,40] ensures the wave vector k_z well within the first BZ to avoid spurious solutions, and is employed in our simulation. This approach relies on the periodicity of a QCL structure along the z direction. The envelope function $\psi^{\Gamma}_{n,j}(z)$ is expanded in a Fourier series[40]

$$\psi^{\Gamma}_{n,j}(z) = \sum_m a^{\Gamma,j}_{mn} e^{iG_m z}, \quad (5)$$

where $G_m = 2m\pi/d$ are the corresponding reciprocal vectors ($m=0, \pm1, \pm2, \cdots$), d denotes the length of two stages, and the index m is an integer, $-N_G \le m \le N_G$ ($N_G=50$ used), which runs over the number of Fourier components retained. Substituting this expression into Eq. (4), multiplying both sides by $e^{-iG_{m'}z}$, and integrating over d, we obtain an approximation to Eq. (4) as the eigenvalue problem

$$\sum_{j,m'} \sum_{j',m} a^{\Gamma,j'}_{mn} \frac{1}{d} \int_0^d dz\, e^{i(G_m - G_{m'})z} [H_{jj'}(G_m, z) + U_{\Gamma}(z)\delta_{jj'}] = E^{\Gamma}_n a^{\Gamma,j}_{m'n}. \quad (6)$$

The matrix element $H_{jj'}(G_m, z)$ has the same form as Eq. (A1) for each layer of material at position z, with k_z replaced by G_m. Equation (6) is a standard eigenvalue problem for the coefficients $a^{\Gamma,j}_{m'n}$ with a super-matrix of size $3(2N_G+1) \times 3(2N_G+1)$. Diagonalization of this matrix then leads to $3(2N_G+1)$ eigenenergies E^{Γ}_n and the corresponding eigenvectors. The top $2N_G+1$ energy levels belong to the conduction subbands, and the associated eigenvectors construct the full subband wave functions. The remaining $2(2N_G+1)$ eigenenergies and eigenvectors characterize the valence subbands, which are not of concern in this work.

After obtaining $\psi^{\Gamma}_{n,j}(z)$, we calculate an average in-plane effective mass for each Γ-conduction subband n

$$\frac{1}{m^*_n} = \sum_j \int_0^d dz \frac{\psi^{\Gamma*}_{n,j}(z)\psi^{\Gamma}_{n,j}(z)}{m^*(j, z)}, \quad (7)$$

where $m^*(j, z)$ is the effective mass of the band j of the material at position z. Based on the new electron effective

mass, the in-plane energy dispersion is regarded as parabolic: $E^{\Gamma}_{n,\mathbf{k}}=E^{\Gamma}_{n}+\hbar^2\mathbf{k}^2/2m^*_n$.

There are two groups of X valleys in (001)-grown QCL structures: the X_z valley along the axis z, and two side valleys X_x, X_y oriented along the x and y directions, respectively. The X_x and X_y valleys are equivalent within the effective-mass framework, and are regarded as one doubly degenerate X_x valley.

In the EFA, near the X-valley minima, the electron wave functions $\Psi^{X_x}_{n,\mathbf{k}}(\mathbf{r},z)$ and $\Psi^{X_z}_{n,\mathbf{k}}(\mathbf{r},z)$ can be expressed by

$$\Psi^{X_x}_{n,\mathbf{k}}(\mathbf{r},z)=\frac{1}{\sqrt{A}}e^{i\left(\mathbf{k}\cdot\mathbf{r}+\frac{\pi}{a}x\right)}\psi^{X_x}_n(z)u^{X_x}(\mathbf{r},z), \tag{8a}$$

$$\Psi^{X_z}_{n,\mathbf{k}}(\mathbf{r},z)=\frac{1}{\sqrt{A}}e^{i\mathbf{k}\cdot\mathbf{r}}\psi^{X_z}_n(z)u^{X_z}(\mathbf{r},z), \tag{8b}$$

where $\psi^{\ell}_n(z)$ ($\ell=X_x$, X_z) are the envelope functions along z, $u^{\ell}(\mathbf{r},z)$ are the Bloch functions, and a is the monolayer width.

To solve for $\psi^{\ell}_n(z)$, the effective-mass equations are sufficient, since the X valleys are well above the valence bands and the effect of valence bands on the X-valley electronic states is negligible. $\psi^{X_x}_n(z)$ and $\psi^{X_z}_n(z)$ in each layer satisfy the effective-mass Eqs. (9a) and (9b), respectively.

$$\left[\frac{-\hbar^2}{2m^*_t(z)}\frac{\mathrm{d}^2}{\mathrm{d}z^2}+U_X(z)\right]\psi^{X_x}_n(z)=E^{X_x}_n\psi^{X_x}_n(z), \tag{9a}$$

$$\left[\frac{-\hbar^2}{2m^*_l(z)}\frac{\mathrm{d}^2}{\mathrm{d}z^2}+U_X(z)\right]\psi^{X_z}_n(z)=E^{X_z}_n\psi^{X_z}_n(z), \tag{9b}$$

where $m^*_t(z)$ and $m^*_l(z)$ are the corresponding transverse and longitudinal X-valley electron effective mass; $U_X(z)=E_X(z)-|e|F(z-d/2)$ is the external potential, where $E_X(z)$ contains the X-valley conduction-band offset relative to a common energy reference level.

In the reciprocal-space approach,[40] following a procedure similar to that described for the Γ-subband envelope function $\psi^{\Gamma}_{n,j}(z)$ [Eqs. (5) and (6)], we obtain the eigenvalue problem

$$\sum_{m',m}a^{X_x}_{mn}\frac{1}{d}\int_0^d \mathrm{d}z\, e^{i(G_m-G_{m'})z}\left[\frac{\hbar^2G^2_m}{2m^*_t(z)}+U_X(z)\right]=E^{X_x}_n a^{X_x}_{m'n}, \tag{10}$$

for the Fourier coefficients $a^{X_x}_{mn}$. The eigenvalue problem for $a^{X_z}_{mn}$ is similar to Eq. (10) with $m^*_t(z)$ replaced by $m^*_l(z)$. Solutions of the eigenvalue problems provide $2N_G+1$ energy levels and the corresponding eigenvectors for the X_x (X_z) subbands, where X_x subbands are doubly degenerate.

With the envelope function $\psi^{\ell}_n(z)$, we compute the average in-plane longitudinal ($m^{\ell *}_{\mathrm{ln}}$) and transverse ($m^{\ell *}_{\mathrm{tn}}$) electron effective mass for each X-subband n

$$\frac{1}{m^{\ell^*}_{\mathrm{in}}}=\int_0^d \mathrm{d}z\frac{|\psi^{\ell}_n(z)|^2}{m^*_i(z)},\quad i=l,\,t. \tag{11}$$

A parabolic in-plane dispersion relation is assumed with the averaged effective mass

TABLE I. Scattering mechanisms included in the Monte Carlo simulation for the Γ- and X-valley states.

	Γ valley	X_x valley	X_z valley
Intrastage ($\lambda\rightarrow\lambda$) & Interstage ($\lambda\rightarrow\lambda\pm1$)	Electron-LO Electron-electron $\Gamma\rightarrow X_x$ $\Gamma\rightarrow X_z$	Electron-LO $X_x\rightarrow\Gamma$ $X_x\rightarrow X_x$ $X_x\rightarrow X_z$	Electron-LO $X_z\rightarrow\Gamma$ $X_z\rightarrow X_x$

$$E^{X_x}_{n,\mathbf{k}}=E^{X_x}_n+\frac{\hbar^2\mathbf{k}^2}{2\sqrt{m^*_{\mathrm{ln}}m^*_{\mathrm{tn}}}}, \tag{12a}$$

$$E^{X_z}_{n,\mathbf{k}}=E^{X_z}_n+\frac{\hbar^2\mathbf{k}^2}{2m^*_{\mathrm{tn}}}. \tag{12b}$$

The above methods of solving for the Γ- and X-subband envelope functions are valid under the assumption that material changes occur slowly. Although this assumption is not true for heterojunctions, where those changes are discontinuous, it is not a bad approximation when we are mostly interested in the regions relatively far from the interfaces. In addition, the above wave functions $\Psi^{\eta}_{n,\mathbf{k}}$ and energy dispersions $E^{\eta}_{n,\mathbf{k}}$ ($\eta=\Gamma$, X_x, X_z) are obtained by treating two adjacent stages as one period. They need to be properly assigned to each stage according to the localization of wave functions. Then the lowest N_η conduction subbands in each stage are selected for transport simulation. N_Γ is set to be 10, and N_{X_x} (N_{X_z}) depends on the applied field and QCL structure. We relabel the chosen electronic states in stage λ as $|\mathbf{k},\,\nu\lambda\eta\rangle$ (νth subband, λth stage, and ηth valley), the associated effective mass as $m^{\eta^*}_{\nu\lambda}$, and the energy dispersion $E^{\eta}_{\nu\lambda}(\mathbf{k})=E_{\mathbf{k}}+E^{\eta}_{\nu\lambda}$ with $E_{\mathbf{k}}=\hbar^2\mathbf{k}^2/2m^{\eta^*}_{\nu\lambda}$. The states $|\mathbf{k},\nu\lambda\eta\rangle$ are rewritten in the form

$$|\mathbf{k},\,\nu\lambda\Gamma\rangle=\frac{1}{\sqrt{A}}e^{i\mathbf{k}\cdot\mathbf{r}}\sum_j\psi^{\Gamma}_{j,\,\nu\lambda}(z)u^{\Gamma}_{j0}(\mathbf{r},z), \tag{13a}$$

$$|\mathbf{k},\,\nu\lambda X_x\rangle=\frac{1}{\sqrt{A}}e^{i\left(\mathbf{k}\cdot\mathbf{r}+\frac{\pi}{a}x\right)}\psi^{X_x}_{\nu\lambda}(z)u^{X_x}(\mathbf{r},z), \tag{13b}$$

$$|\mathbf{k},\,\nu\lambda X_z\rangle=\frac{1}{\sqrt{A}}e^{i\mathbf{k}\cdot\mathbf{r}}\psi^{X_z}_{\nu\lambda}(z)u^{X_z}(\mathbf{r},z). \tag{13c}$$

The subband index $\nu=1,2,\ldots,N_\eta$ for valley η. Similar notation is used for the electronic states in stage $\lambda+1$.

B. Scattering mechanisms

The various scattering mechanisms included in the Monte Carlo simulation are listed in Table I. An intervalley scattering mechanism is written in the form A→B (e.g., $\Gamma\rightarrow X_x$) in the table, with A being the initial valley and B the final valley. The electron-LO phonon scattering is included for all the valleys, but the electron-electron (e-e) interaction is implemented only for the Γ states. The intervalley scattering $X_x\rightarrow X_x$ takes place due to the double-degeneracy of the X_x states. For all the scattering mechanisms, we include both the intrastage and interstage scattering events, with the latter

yielding the current flow through the QCL. The scattering rates are computed assuming empty final states, and the interstage $\lambda \rightarrow \lambda - 1$ scattering rates are computed through the interstage $\lambda + 1 \rightarrow \lambda$ scattering due to the translational symmetry. The Pauli exclusion principle for the final states is included in the EMC code following the rejection technique by Lugli.[41]

1. Electron-LO phonon scattering

The scattering of electrons with longitudinal polar optical phonons in a multiple-quantum-well (MQW) system is usually described by the Fröhlich interaction. Though electrons have been widely accepted as quasi-two-dimensional (2D) particles in such systems, the correct model for the lattice vibrational modes is still an area of active research. A microscopic calculation[42] indicated a great effect of confinement on the phonon dispersion, and the presence of interface modes in quantum-well systems. While these modifications have important consequences for time-resolved phonon spectroscopy, they are far less crucial for transport phenomena. The assumption of dispersionless unscreened bulk phonon modes has been shown[42] to reproduce the total scattering rate sufficiently well, and is taken in our calculation of the electron-LO phonon scattering rates.

The transition rate from a state $|\mathbf{k},\ \nu\lambda\,\eta\rangle$ to a new state $|\mathbf{k}',\ \nu'\lambda'\,\eta\rangle$ (λ' could be λ, $\lambda+1$, or $\lambda-1$) is given by Fermi's golden rule

$$S_{\nu\lambda\,\eta}^{\nu'\lambda'\,\eta}(\mathbf{k},\,\mathbf{k}') = \frac{2\pi}{\hbar}|\langle \mathbf{k}',\ \nu'\lambda'\,\eta|H_{\text{e-LO}}|\mathbf{k},\ \nu\lambda\,\eta\rangle|^2 \times \delta(E' - E \mp \hbar\omega_0), \tag{14}$$

where $\hbar\omega_0$ is the LO phonon energy, $\delta(\cdot)$ is the delta function, and the upper and lower signs correspond to phonon absorption and emission, respectively (this convention will be used throughout this section). The total scattering rate for an electron initially in subband ν, stage λ, to a final subband ν', stage λ', may be written[30,43] as

$$\Lambda_{\nu\lambda\,\eta}^{\nu'\lambda'\,\eta}(\mathbf{k}) = \sum_{\mathbf{k}'} S_{\nu\lambda\,\eta}^{\nu'\lambda'\,\eta}(\mathbf{k},\,\mathbf{k}') = \frac{e_0^2\hbar\omega_0 m_{\nu'\lambda'}^{\eta*}}{8\pi\hbar^3} \times \left(n_0 + \frac{1}{2} \mp \frac{1}{2}\right)\left(\frac{1}{\varepsilon_\infty} - \frac{1}{\varepsilon_0}\right) \times \int_0^{2\pi} \mathrm{d}\theta \frac{F_{\nu\lambda\,\eta}^{\nu'\lambda'\,\eta}(q^\pm)}{q^\pm} \times \vartheta(E_{\mathbf{k}} + E_{\nu\lambda}^{\eta} - E_{\nu'\lambda'}^{\eta} \pm \hbar\omega_0), \tag{15}$$

where n_0 is the equilibrium phonon number, ε_0 and ε_∞ are the low- and high-frequency dielectric constants, $q = |\mathbf{k}' - \mathbf{k}|$, θ is the angle between $\mathbf{k}$ and $\mathbf{k}'$, and $\vartheta(\cdot)$ is the Heaviside step function.

The form factor function $F_{\nu\lambda\,\eta}^{\nu'\lambda'\,\eta}(q)$ depends on the valleys. For the Γ valley, since the electron wave functions include the influence of the valence bands (Sec. II A), we calculate the form factor function by averaging over the elementary cell and employing the orthogonality of the zone-center Bloch functions $u_{j0}(\mathbf{r},\ z)$ (j=c, lh, so). Then we obtain

$$F_{\nu\lambda\Gamma}^{\nu'\lambda'\Gamma}(q) = \sum_{j,\,j'} \int_0^d \mathrm{d}z \int_0^d \mathrm{d}z'\ \psi_{j,\ \nu'\lambda'}^{\Gamma}(z)\psi_{j',\ \nu'\lambda'}^{\Gamma*}(z') \times \psi_{j,\ \nu\lambda}^{\Gamma*}(z)\psi_{j',\ \nu\lambda}^{\Gamma}(z')e^{-q|z-z'|}. \tag{16}$$

For $\ell = \mathrm{X}_x,\ \mathrm{X}_z$ valleys, the form factor is calculated using the envelope functions as

$$F_{\nu\lambda\ell}^{\nu'\lambda'\ell}(q) = \int_0^d \mathrm{d}z \int_0^d \mathrm{d}z'\ \psi_{\nu'\lambda'}^{\ell}(z)\psi_{\nu'\lambda'}^{\ell*}(z')\psi_{\nu\lambda}^{\ell*}(z) \times \psi_{\nu\lambda}^{\ell}(z')e^{-q|z-z'|}. \tag{17}$$

The allowed q's are fixed by the energy and in-plane momentum conservation laws. Taking into account the difference of the electron effective mass between the initial and final states, we have

$$q^\pm = \frac{\sqrt{2}}{\hbar}\{(m_{\nu\lambda}^{\eta*} + m_{\nu'\lambda'}^{\eta*})E_{\mathbf{k}} + m_{\nu'\lambda'}^{\eta*}(\hbar\omega_{\nu\nu'}^{\pm}) - 2[m_{\nu\lambda}^{\eta*}m_{\nu'\lambda'}^{\eta*}E_{\mathbf{k}}(E_{\mathbf{k}} + \hbar\omega_{\nu\nu'}^{\pm})]^{1/2}\cos\theta\}^{1/2}, \tag{18}$$

with $\hbar\omega_{\nu\nu'}^{\pm} = E_{\nu\lambda}^{\eta} - E_{\nu'\lambda'}^{\eta} \pm \hbar\omega_0$.

2. Intervalley scattering

It has been shown[44] that the phonon-assisted intervalley electron transitions can be modeled through the intervalley deformation potential (DP). For bulk intervalley phonons, the total intervalley scattering rate for an electron from a state $|\mathbf{k},\ \nu\lambda\,\eta\rangle$ to a state of subband ν', stage λ', valley η' is given by[43]

$$\Lambda_{\nu\lambda\,\eta}^{\nu'\lambda'\,\eta'}(\mathbf{k}) = \frac{Z_{\eta'}D_{\eta\eta'}^2 m_{\nu'\lambda'}^{\eta'*}}{2\hbar\rho E_{\eta\eta'}}\left(n_{\eta\eta'} + \frac{1}{2} \mp \frac{1}{2}\right)I_{\nu\lambda\,\eta}^{\nu'\lambda'\,\eta'}\vartheta \times (E_{\mathbf{k}} + E_{\nu\lambda}^{\eta} - E_{\nu'\lambda'}^{\eta'} \pm E_{\eta\eta'}), \tag{19}$$

where $D_{\eta\eta'}$ is the intervalley ($\eta - \eta'$) deformation potential constant, ρ is the mass density, and $E_{\eta\eta'}$ is the intervalley phonon energy; $n_{\eta\eta'}$ is the equilibrium intervalley phonon occupancy, and $Z_{\eta'}$ is the degeneracy of the final valley ($Z_\Gamma = 1$, $Z_{X_z} = 1$, and $Z_{X_x} = 1$ for intervalley $X_x - X_x$, two for others). The overlap integral $I_{\nu\lambda\,\eta}^{\nu'\lambda'\,\eta'}$ is given by

$$I_{\nu\lambda\Gamma}^{\nu'\lambda'\ell} = \sum_j \int_0^d \mathrm{d}z|\psi_{j,\nu\lambda}^{\Gamma}(z)|^2|\psi_{\nu'\lambda'}^{\ell}(z)|^2, \tag{20a}$$

$$I_{\nu\lambda\ell}^{\nu'\lambda'\ell'} = \int_0^d \mathrm{d}z|\psi_{\nu\lambda}^{\ell}(z)|^2|\psi_{\nu'\lambda'}^{\ell'}(z)|^2, \tag{20b}$$

where the first equation is for the scattering between Γ and ℓ ($\ell = X_x,\ X_z$) valleys, and the second one is for the intervalley scattering among the X valleys. All the material constants necessary for calculating scattering rates are borrowed from GaAs.[45]

3. Electron-electron scattering

The electron-electron (e-e) scattering among the Γ subbands has a significant effect[20] on QCL structures. We include the e-e scattering for the Γ subbands, but not for the X subbands, since the electron densities in the X valleys are pretty low except at high fields (above threshold). The e-e interaction may be divided into the binary e-e scattering and electron-plasmon coupling, with the latter being important in highly-doped systems and neglected in our calculation. The binary quasi-2D e-e scattering is treated by taking into account both the antiparallel-spin and parallel-spin e-e collisions, with the exchange effect[46] included for the parallel-spin collisions.

We consider a "principal" Γ-electron in subband ν, stage λ, with an in-plane wave vector $\mathbf{k}$, and a "partner" Γ electron in subband μ, stage λ_0, with a wave vector $\mathbf{k}_0$. Since the e-e scattering involves only the Γ valley, we will omit the valley index in the following. The final states of these two electrons are $|\mathbf{k}', \nu'\lambda'\rangle$ and $|\mathbf{k}_0', \mu'\lambda_0'\rangle$, respectively. The total electron scattering rate from the state $|\mathbf{k}, \nu\lambda\rangle$ into a final state of subband ν', stage λ′, is given by[47]

$$\Lambda_{\nu\lambda}^{\nu'\lambda'}(\mathbf{k}) = \frac{e_0^4 m_{\nu\lambda}^*}{32\pi\hbar^3\varepsilon_\infty^2 A}\sum_{\mathbf{k}_0,\sigma}\sum_{\mu\mu'}\sum_{\lambda_0\lambda_0'} f_{\mu\lambda_0}(\mathbf{k}_0)\int_0^{2\pi} d\theta\left[\frac{|F(q)|^2}{q^2\varepsilon^2(q)} + \frac{|F(q')|^2}{q'^2\varepsilon^2(q')} - \frac{|F(q)||F(q')|}{q\varepsilon(q)q'\varepsilon(q')}\right], \quad (21)$$

where σ denotes the spin of electrons, $f_{\mu\lambda_0}(\mathbf{k}_0)$ is the Γ valley electron distribution, θ is the angle between $\mathbf{g}$ $(\mathbf{g}=\mathbf{k}_0-\mathbf{k})$ and $\mathbf{g}'$ $(\mathbf{g}'=\mathbf{k}_0'-\mathbf{k}')$, $q=|\mathbf{g}-\mathbf{g}'|/2$, and $\varepsilon(q)$ is the static dielectric function; each of the three indices $(\lambda', \lambda_0, \lambda_0')$ could be λ, $\lambda+1$, or $\lambda-1$. The form factor function $F(q)$ (with indices omitted for compactness) satisfies

$$F_{\nu\mu\nu'\mu'}^{\lambda\lambda_0\lambda'\lambda_0'}(q) = \sum_{i,j}\int_0^d dz\int_0^d dz'\ \psi_{i,\nu\lambda}^{\Gamma}(z)\psi_{i,\nu'\lambda'}^{\Gamma*}(z) \times \psi_{j,\mu\lambda_0}^{\Gamma}(z')\psi_{j,\mu'\lambda_0'}^{\Gamma*}(z')e^{-q|z-z'|}, \quad (22)$$

with i and j both running over the three bands (c, lh, so) at the zone-center. The values of q and q' are determined by

$$q = \frac{1}{2}[2g^2 + g_0^2 - 2g\sqrt{g^2+g_0^2}\cos\theta]^{1/2}, \quad (23a)$$

$$q' = \frac{1}{2}[2g^2 + g_0^2 + 2g\sqrt{g^2+g_0^2}\cos\theta]^{1/2}, \quad (23b)$$

where

$$g = |\mathbf{g}|,\ \ g_0 = \frac{2}{\hbar}[m_{\nu\lambda}^{\Gamma*}(E_{\nu\lambda}^{\Gamma} + E_{\mu\lambda_0}^{\Gamma} - E_{\nu'\lambda'}^{\Gamma} - E_{\mu'\lambda_0'}^{\Gamma})]^{1/2}. \quad (24)$$

Analysis of the screening phenomena in multisubband systems, such as QCLs, is a formidable task. We treat the effect of multisubband screening within the static random-phase approximation (RPA). In the long-wavelength limit $q\to 0$, for intrasubband $(\nu=\nu',\ \lambda=\lambda',\ \mu=\mu',\ \lambda_0=\lambda_0')$ e-e transitions, the static dielectric function may be written as[48]

$$\varepsilon(q) = 1 + \sum_{\nu=1}^{N_\Gamma} f_{\nu\lambda}(0)\frac{q_{\nu\lambda}}{q},\ \ q_{\nu\lambda} = \frac{e_0^2 m_{\nu\lambda}^{\Gamma*}}{2\pi\hbar^2\varepsilon_\infty}, \quad (25)$$

where $f_{\nu\lambda}(0)$ is the occupancy of the bottom of the subband ν in the central stage λ. The occupancy $f_{\nu\lambda}(0)$ is evaluated at each time step in the EMC simulation, and independent of whether the distribution function is the equilibrium one. This fact allows for the screening function to be adjusted according to the actual electron distribution.

For intersubband e-e scattering, the effect of screening is expected to be much less than for the intrasubband case, since the dielectric function is weighted by the form factor functions within the RPA, and the intersubband form factors are much lower in magnitude and vanish for $q=0$, due to the orthogonality of the envelope functions. Therefore, to first order, we treat the intersubband e-e scattering as unscreened, which is also validated by Fig. 3 of Ref. 23, where the unscreened intersubband Coulomb potential is very close to their screened potential.

The implementation of the e-e interaction in the EMC code follows the technique by Goodnick and Lugli:[49] We precalculate the form factors as a function of q according to Eq. (22), then compute the scattering rate $\Lambda_{\nu\lambda}^{\nu'\lambda'}(\mathbf{k})$ in Eq. (21) by replacing the integrand with the square of the maximum value of $F_{\nu\mu\nu'\mu'}^{\lambda\lambda_0\lambda'\lambda_0'}(q)$ for given $\nu\lambda, \nu'\lambda'$, divided by $q_{\nu\lambda}^2$ given in Eq. (25); the actual value of the integrand function is accounted for through a rejection method when the final state is chosen. The scattering rate employed in the simulation is computed using half of the rate in Eq. (21), since each carrier from the simulated ensemble is scattered both as a principal electron and as a scattering partner.[50] In addition, it is necessary to update both the principal electron and its partner electron after the e-e collisions, in order to conserve the energy and momentum in the system.[50]

III. RESULTS AND DISCUSSION

Figure 2 shows the Γ-subband energy levels and wave function moduli squared in two adjacent stages for the 33% QCL [Fig. 2(a)] and the 45% QCL [Fig. 2(b)] at the above-threshold field $F=53$ kV/cm and $T=77$ K. In each stage, ten Γ subbands, including two Γ-continuum (Γ_c) states, are used in the simulation for both lasers. The X subbands under the same condition are displayed in Fig. 3 with the Γ_c states also plotted, where Fig. 3(a) is for the 33% QCL and Fig. 3(b) for the 45% case. The number of X states in each stage is identical and chosen such that the highest X subband is right above the second Γ_c state and below other higher X levels. Since the X band edge is about 83 meV above the Γ band edge in the 33% QCL, but ~30 meV below in the 45% QCL, more X subbands are needed to properly simulate the latter device. In particular, at $F=53$ kV/cm and $T=77$ K, nine (ten) X_z subbands and four (six) X_x subbands are used in the 33% (45%) QCL simulation.

The applied field versus current density characteristics at the temperatures of 77 and 300 K are shown in Fig. 4 for the 33% QCL [Fig. 4(a)] and the 45% QCL [Fig. 4(b)], with and without the X-valley transport included. (Note that the leakage to Γ-continuum states[51] is accounted for as part of the

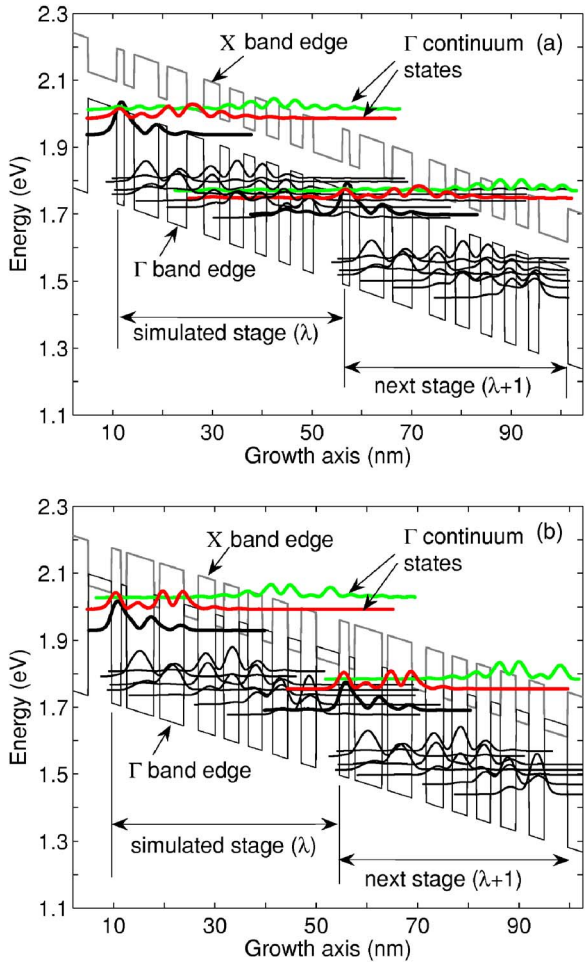

FIG. 2. (Color online) Γ-subband energy levels and wave function moduli squared in two adjacent stages for the 33% QCL (a) and the 45% QCL (b) at $F=53$ kV/cm (above-threshold) and $T=77$ K. In each stage, the bold black line denotes the upper lasing level, and the thin ones are the localized states (Γ_l), and the top two (red and green) are the continuum states (Γ_c).

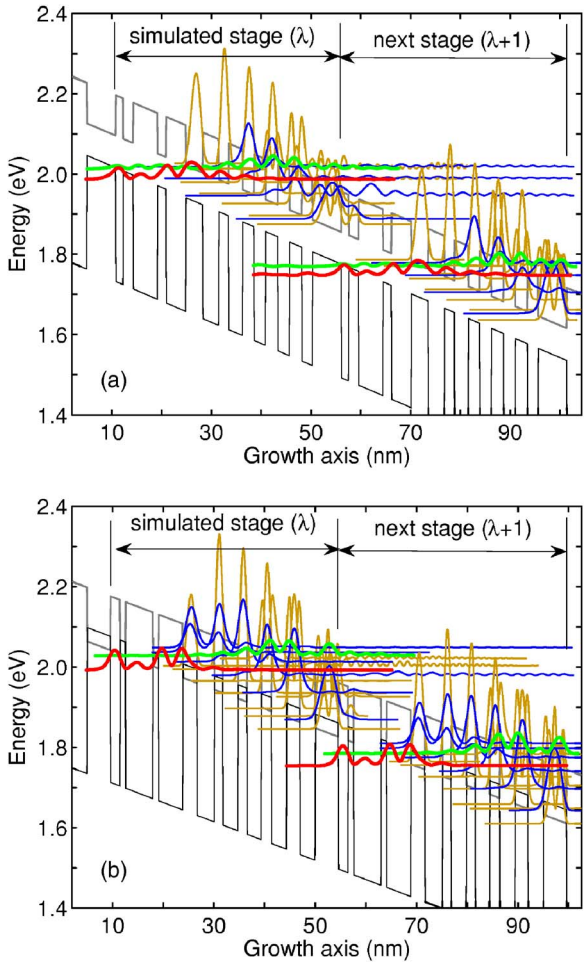

FIG. 3. (Color online) X-subband energy levels and wave function moduli squared in two adjacent stages for the 33% QCL (a) and the 45% QCL (b) at $F=53$ kV/cm and $T=77$ K. The blue lines denote the X_x states, and the yellow ones are the X_z states, while the red and green lines are the Γ_c subbands.

Γ-valley current, so it is present in both curves.) The calculated J_{th} at $F=48$ kV/cm are summarized in Table II, together with the available experimental data. It can be seen that the calculated J_{th} values are in very good agreement with the experimental data, considering that the simulation does not account for the losses at the lateral waveguide (ridge) edges. Subsequent experimental work[16] on 45% QCLs, where the ridge edges had smooth surfaces due to wet chemical etching, and no absorbing material, reported J_{th} (77 K) $=3$ kA/cm^2, in excellent agreement with 2.9 kA/cm^2 obtained in our calculation.

At the cryogenic temperature, the inclusion of the X-valley transport has a very negligible effect on the current density up to above-threshold fields in both QCLs, but the 33% QCL shows about 1 kA/cm^2 higher J_{th} than the 45% QCL in both theory and experiment. This difference is primarily due to strong $\Gamma_l \rightarrow \Gamma_c$ interstage leakage, stemming from poor localization of the Γ_l states in the 33% QCL and their large overlap with the next-stage Γ_c states [Fig. 2(a)]. This overlap is much smaller in the 45% device, thanks to the higher Γ barriers, as seen in Fig. 2(b). This mechanism of leakage via the Γ_c states has been well known[4,16,17] and studied theoretically.[19] At room temperature, the X-valley leakage current is very large in the 33% QCL, even at fields significantly below threshold, equaling 8.3 kA/cm^2 at threshold.

Figure 5 presents the variation of the electron population in Γ and X valleys with the field at different temperatures. By comparing Figs. 4 and 5 at 300 K, we observe that the increase in the X-valley leakage current in both lasers follows the increase in the X-valley population (also true at 77 K, although somewhat less obvious). This is due to the fact that interstage $X \rightarrow X$ intervalley scattering is the dominant leakage mechanism in both QCLs, more efficient than direct interstage scattering between Γ and X. The dominant X-valley leakage takes place through the three-step process sketched in Fig. 6. First of all, the coupling between the Γ_l and the next-stage Γ_c states results in the leakage current J_c. Once those continuum states are populated, electrons will efficiently scatter into the X valleys, because the X states have larger masses and are strongly coupled to the Γ_c states in both QCLs, as seen from their large wave function overlap in Fig. 3. After electrons get into the X valleys, they tend not to scatter back to the Γ valley, because of the lighter effective mass of the Γ_c states. What happens next is that the plane-wavelike tails of the X wave functions in the simulated stage

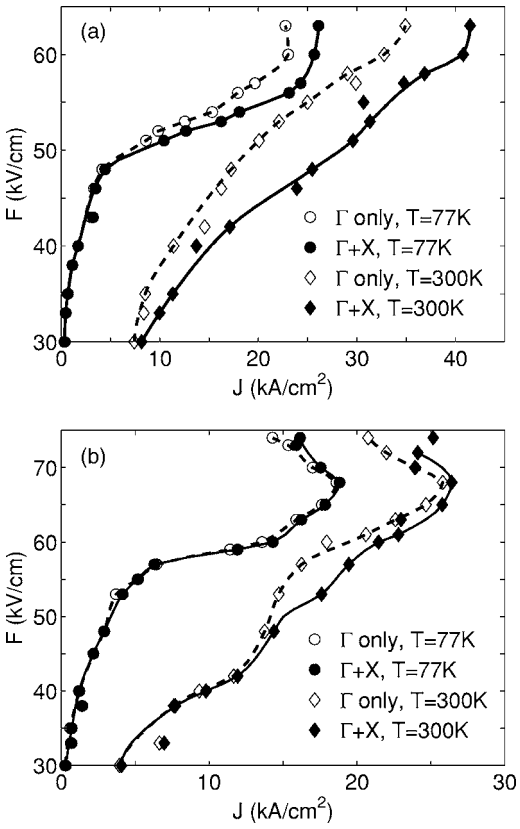

FIG. 4. Electric field vs current density characteristics for the 33% QCL (a) and the 45% QCL (b) at 77 and 300 K, with and without the *X*-valley transport included.

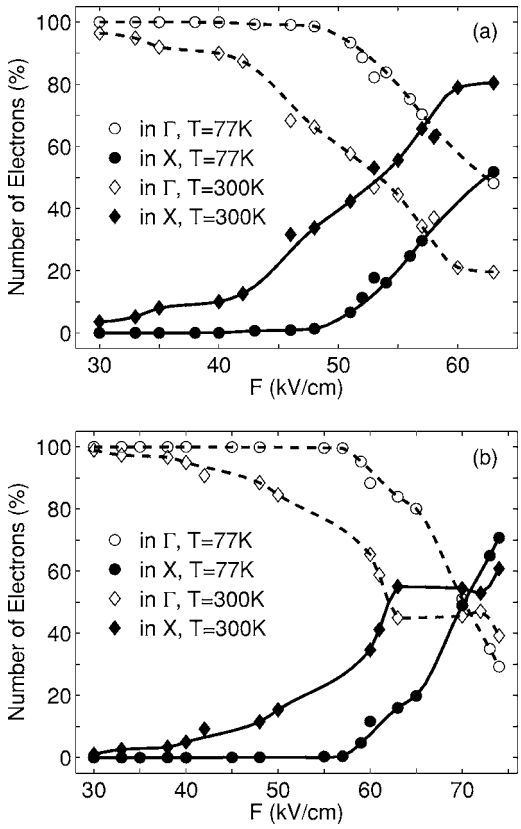

FIG. 5. Electron population in Γ and *X* valleys vs field for the 33% QCL (a) and the 45% QCL (b) at 77 and 300 K.

couple to the *X* states in the next stage (also seen in Fig. 3), giving rise to the interstage *X*-to-*X* leakage current J_X. Other leakage paths, e.g., from Γ_l to the next-stage *X* states, are less efficient.

After identifying the dominant *X*-valley leakage mechanism, we are in the position to explain why there is a large *X*-valley leakage current J_X in the 33% QCL at room temperature even at low fields, but not in the 45% device. The value of J_X relies on the *X*-valley population and the number of intervalley *X*-*X* phonons. In the 33% QCL, at room temperature, the leakage J_c is very strong, due to both the large wave function overlap and the increase in the number of the polar optical phonons, which leads to high Γ_c population. At the same time, the number of intervalley Γ-to-*X* phonons increases. The combination of these two factors results in highly efficient scattering from Γ_c to the same-stage *X* states (black arrow in Fig. 6), implying high-*X*-valley population, since the scattering process efficiency depends on the number of phonons as well as the initial occupation. In addition, the number of intervalley *X*-*X* phonons is also raised. Consequently, the intervalley *X*-*X* scattering from the simulated stage to the next stage is greatly enhanced, producing a large J_X. In the 45% QCL, in contrast, Γ_c does not get filled through $\Gamma_l \rightarrow \Gamma_c$ interstage scattering because their overlap is very small, which explains the near-zero J_X below threshold [Fig. 4(b)]. Only at very high fields, Γ_c gets filled by intrastage scattering (i.e., high fields lead to high-electronic temperatures), which then augments the leakage current J_X to some extent. The mechanism of *X*-valley leakage described above holds at 77 K as well, but leakage is much less pronounced because of few active phonons that enable intervalley scattering.

TABLE II. Calculated threshold current densities J_{th} with and without the *X*-valley transport included.

	J_{th} (kA/cm^2), 77 K			J_{th} (kA/cm^2), 300 K		
	Without *X*	With *X*	Experiment	Without *X*	With *X*	Experiment
33% QCL	4.1	4.4	5.0[a]	17.2	25.5	N/A
45% QCL	2.9	2.9	4.0[b]	13.7	14.4	16.7[b]

[a]Reference 2.
[b]Reference 4.

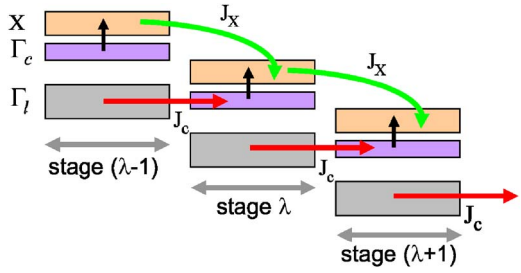

FIG. 6. (Color online) Schematic of the dominant *X*-valley leakage mechanism in both QCLs.

IV. SUMMARY

A detailed Monte Carlo simulation including both Γ- and *X*-valley transport has been developed and used to investigate the effects of *X*-valley transport on equivalent-design GaAs/$Al_{0.33}Ga_{0.67}As$ (33% QCL) and GaAs/$Al_{0.45}Ga_{0.55}As$ (45% QCL) mid-IR QCLs. Simulation reveals that the dominant *X*-valley leakage path in both QCLs is the interstage $X \rightarrow X$ intervalley scattering, causing a parallel leakage current J_X. The magnitude of J_X depends on the temperature and occupation of the *X*-valley subbands, which are populated primarily by the same-stage scattering from the Γ-continuum (Γ_c) states. In the 33% QCL, Γ-localized (Γ_l) states are strongly coupled to the next-stage Γ_c. Not only does this coupling lead to the well-recognized $\Gamma_l \rightarrow \Gamma_c$ leakage, but also, through populating Γ_c, indirectly ensures high-*X*-valley occupation and subsequent strong interstage $X \rightarrow X$ scattering. Consequently, at room temperature, the leakage current J_X is very high in the 33% QCL, even at fields below threshold. In contrast, in the 45% QCL, coupling of Γ_l with the next-stage Γ_c is weak, due to good localization of the Γ_l states coming from the high barriers. Consequently, occupation of the *X* states through the same-stage $\Gamma_c \rightarrow X$ scattering is low, leading to small J_X up to high fields. The simulated J_{th} with the *X*-valley leakage included is in very good agreement with experiment for both QCLs at 77 and 300 K. This realistic simulator can be readily adapted to account for the indirect-valley leakage in InP-based structures, thereby becoming a versatile aid in the design of mid and far-infrared QCLs.

ACKNOWLEDGMENT

This work has been supported by the Wisconsin Alumni Research Foundation (WARF).

APPENDIX

In this Appendix, we reproduce the three-band $\mathbf{K}\cdot\mathbf{p}$ Hamiltonian matrix elements with only the parameters relevant to our work. With the in-plane wave vector $\mathbf{k}=0$, the eight-band $\mathbf{K}\cdot\mathbf{p}$ Hamiltonian matrix[34] reduces to a 6×6 matrix, with the hh band factoring out. Due to the spin degeneracy, this 6×6 matrix can be reduced to a 3×3 matrix, which takes the form of

$$H_{3\times3}=\begin{bmatrix} E_c+(1+2F_K)E_z+A_\varepsilon & \sqrt{\frac{2}{3}E_PE_z} & \sqrt{\frac{1}{3}E_PE_z} \\ \sqrt{\frac{2}{3}E_PE_z} & E_v-(\gamma_1+2\gamma_2)E_z-P_\varepsilon+Q_\varepsilon & -2\sqrt{2}\gamma_2E_z+\sqrt{2}Q_\varepsilon \\ \sqrt{\frac{1}{3}E_PE_z} & -2\sqrt{2}\gamma_2E_z+\sqrt{2}Q_\varepsilon & E_v-\Delta_{so}-\gamma_1E_z-P_\varepsilon \end{bmatrix}, \tag{A1}$$

where

$$E_z=\frac{\hbar^2k_z^2}{2m_0},$$

$$E_P=\frac{2m_0}{\hbar^2}P_{cv}^2,$$

$$P_{cv}=\frac{\hbar}{m_0}\langle iS|p_x|X\rangle,$$

$$\gamma_1=\gamma_1^L-\frac{E_P}{3E_g},$$

$$\gamma_2=\gamma_2^L-\frac{E_P}{6E_g},$$

$$A_\varepsilon=a_c(\varepsilon_{xx}+\varepsilon_{yy}+\varepsilon_{zz}),$$

$$P_\varepsilon=-a_v(\varepsilon_{xx}+\varepsilon_{yy}+\varepsilon_{zz}),$$

$$Q_\varepsilon=-\frac{b}{2}(\varepsilon_{xx}+\varepsilon_{yy}-2\varepsilon_{zz}). \tag{A2}$$

E_c and E_v are the unstrained conduction- and valence-band edges, respectively, relative to a common reference energy. Δ_{so} is the spin-orbit split-off energy. γ_1 and γ_2 are the modified Luttinger parameters,[52] and γ_1^L and γ_2^L are the standard Luttinger parameters.[53] The explicit inclusion of the interaction between the valence and conduction bands in the $\mathbf{K}\cdot\mathbf{p}$ model leads to the modified Luttinger parameters discussed by Pidgeon and Brown.[52] F_K represents[54] the contribution of higher-conduction bands to the effective mass of the Γ_6 conduction-band electrons. P_{cv} is the interband momentum matrix element defined by Kane,[54] and E_P is the energy parameter for P_{cv}. a_c, a_v, and b are the Bir-Pikus deformation potentials,[55] with the sign conventions being negative, positive, and negative, respectively.

For a strained semiconductor layer pseudomorphically grown on a (001)-oriented (*z* axis) substrate, the strain tensor components are[31]

$$\varepsilon_{xx} = \varepsilon_{yy} = \frac{a_0 - a}{a},$$

$$\varepsilon_{zz} = -\frac{2c_{12}}{c_{11}}\varepsilon_{xx}, \tag{A3}$$

$$\varepsilon_{xy} = \varepsilon_{yz} = \varepsilon_{zx} = 0,$$

where a_0 and a are the lattice constants of the substrate and the layer material, respectively, and c_{11} and c_{12} are the elastic stiffness constants of the strained layer. Therefore, A_ε, P_ε, and Q_ε are simplified to

$$A_\varepsilon = 2a_c\left(1 - \frac{c_{12}}{c_{11}}\right)\varepsilon_{xx},$$

$$P_\varepsilon = -2a_v\left(1 - \frac{c_{12}}{c_{11}}\right)\varepsilon_{xx}, \tag{A4}$$

$$Q_\varepsilon = -b\left(1 + \frac{2c_{12}}{c_{11}}\right)\varepsilon_{xx}$$

The material parameters for most III-V semiconductors are documented in Ref. 56.

[1] C. Sirtori, P. Kruck, S. Barbieri, P. Collot, J. Nagle, M. Beck, J. Faist, and U. Oesterle, Appl. Phys. Lett. **73**, 3486 (1998).
[2] C. Sirtori, P. Kruck, S. Barbieri, H. Page, J. Nagle, M. Beck, J. Faist, and U. Oesterle, Appl. Phys. Lett. **75**, 3911 (1999).
[3] H. Page, A. Robertson, C. Sirtori, C. Becker, G. Glastre, and J. Nagle, IEEE Photon. Technol. Lett. **13**, 556 (2001).
[4] H. Page, C. Becker, A. Robertson, G. Glastre, V. Ortiz, and C. Sirtori, Appl. Phys. Lett. **78**, 3529 (2001).
[5] H. Page, P. Collot, A. Rossi, V. Ortiz, and C. Sirtori, Semicond. Sci. Technol. **17**, 1312 (2002).
[6] S. Anders, W. Schrenk, E. Gornik, and G. Strasser, Appl. Phys. Lett. **80**, 1864 (2002).
[7] C. Pflügl, W. Schrenk, S. Anders, G. Strasser, C. Becker, C. Sirtori, Y. Bonetti, and A. Muller, Appl. Phys. Lett. **83**, 4698 (2003).
[8] H. Page, S. Dhillon, M. Calligaro, V. Ortiz, and C. Sirtori, Electron. Lett. **39**, 1053 (2003).
[9] H. Page, S. Dhillon, M. Calligaro, C. Becker, V. Ortiz, and C. Sirtori, IEEE J. Quantum Electron. **40**, 665 (2004).
[10] C. Becker, C. Sirtori, H. Page, G. Glastre, V. Ortiz, X. Marcadet, M. Stellmacher, and J. Nagle, Appl. Phys. Lett. **77**, 463 (2000).
[11] W. Schrenk, N. Finger, S. Gianordoli, E. Gornik, and G. Strasser, Appl. Phys. Lett. **77**, 3328 (2000).
[12] L. R. Wilson, D. A. Carde, J. W. Cockburn, R. P. Green, D. G. Revin, M. J. Steer, M. Hopkinson, G. Hill, and R. Airey, Appl. Phys. Lett. **81**, 1378 (2002).
[13] M. Beck, D. Hofstetter, T. Aellen, J. Faist, U. Oesterle, M. Ilegems, E. Gini, and H. Melchior, Science **295**, 301 (2002).
[14] A. Evans, J. S. Yu, J. David, L. Doris, K. Mi, S. Slivken, and M. Razeghi, Appl. Phys. Lett. **84**, 314 (2004).
[15] S. Blaser, D. A. Yarekha, L. Hvozdara, Y. Bonetti, A. Muller, M. Giovannini, and J. Faist, Appl. Phys. Lett. **86**, 041109 (2005).
[16] C. Sirtori, H. Page, C. Becker, and V. Ortiz, IEEE J. Quantum Electron. **38**, 547 (2002).
[17] S. Barbieri, C. Sirtori, H. Page, M. Stellmacher, and J. Nagle, Appl. Phys. Lett. **78**, 282 (2001).
[18] W. T. Masselink, M. P. Semtsiv, S. Dressler, M. Ziegler, N. Georgiev, T. Dekorsy, and M. Helm, Proc. SPIE **5738**, 13 (2005).
[19] D. Indjin, P. Harrison, R. W. Kelsall, and Z. Ikonić, Appl. Phys. Lett. **81**, 400 (2002).
[20] R. C. Iotti and F. Rossi, Phys. Rev. Lett. **87**, 146603 (2001).
[21] R. C. Iotti and F. Rossi, Semicond. Sci. Technol. **19**, S323 (2004).
[22] H. Callebaut, S. Kumar, B. S. Williams, Q. Hu, and J. L. Reno, Appl. Phys. Lett. **84**, 645 (2004).
[23] O. Bonno, J. L. Thobel, and F. Dessenne, J. Appl. Phys. **97**, 043702 (2005).
[24] V. D. Jovanović, D. Indjin, N. Vukmirović, Z. Ikonić, P. Harrison, and E. H. Linfield, Appl. Phys. Lett. **86**, 211117 (2005).
[25] S. C. Lee and A. Wacker, Phys. Rev. B **66**, 245314 (2002).
[26] S. C. Lee, F. Banit, M. Woerner, and A. Wacker, Phys. Rev. B **73**, 245320 (2006).
[27] F. Eickemeyer, K. Reimann, M. Woerner, and T. Elsaesser, Phys. Rev. Lett. **89**, 047402 (2002).
[28] M. Woerner, K. Reimann, and T. Elsaesser, J. Phys.: Condens. Matter **16**, R25 (2004).
[29] X. Gao, D. Botez, and I. Knezevic, Appl. Phys. Lett. **89**, 191119 (2006).
[30] C. Jacoboni and P. Lugli, *The Monte Carlo Method for Semiconductor Device Simulation* (Springer, New York, 1989).
[31] S. L. Chuang, *Physics of Optoelectronic Devices* (Wiley Interscience, New York, 1995).
[32] J. Faist, F. Capasso, D. L. Sivco, A. L. Hutchinson, S. G. Chu, and A. Y. Cho, Appl. Phys. Lett. **72**, 680 (1998).
[33] L. R. Ram-Mohan, K. H. Yoo, and R. L. Aggarwal, Phys. Rev. B **38**, 6151 (1988).
[34] G. Liu and S. L. Chuang, Phys. Rev. B **65**, 165220 (2002).
[35] B. Chen, M. Lazzouni, and L. R. Ram-Mohan, Phys. Rev. B **45**, 1204 (1992).
[36] X. Cartoixá, D. Z.-Y. Ting, and T. C. McGill, J. Appl. Phys. **93**, 3974 (2003).
[37] L. R. Ram-Mohan, K. H. Yoo, and J. Moussa, J. Appl. Phys. **95**, 3081 (2004).
[38] F. Szmulowicz, Phys. Rev. B **71**, 245117 (2005).
[39] S. Barbieri, F. Beltram, and F. Rossi, Phys. Rev. B **60**, 1953 (1999).
[40] B. Vinter, Phys. Rev. B **66**, 045324 (2002).
[41] P. Lugli and D. K. Ferry, IEEE Trans. Electron Devices **ED-32**, 2431 (1985).
[42] H. Rücker, E. Molinari, and P. Lugli, Phys. Rev. B **45**, 6747 (1992).
[43] S. M. Goodnick and P. Lugli, *Hot Carriers in Semiconductor Nanostructures* (Academic, New York, 1992).
[44] O. E. Raichev, Phys. Rev. B **49**, 5448 (1994).
[45] M. Lundstrom, *Fundamentals of Carrier Transport* (University Press, Cambridge, 2000).
[46] A. Mošková and M. Moško, Phys. Rev. B **49**, 7443 (1994).
[47] M. Moško, A. Mošková, and V. Cambel, Phys. Rev. B **51**, 16860 (1995).
[48] S. M. Goodnick and P. Lugli, Appl. Phys. Lett. **51**, 584 (1987).
[49] S. M. Goodnick and P. Lugli, Phys. Rev. B **37**, 2578 (1988).
[50] M. Moško and A. Mošková, Phys. Rev. B **44**, 10794 (1991).
[51] D. Indjin, P. Harrison, R. W. Kelsall, and Z. Ikonić, J. Appl. Phys. **91**, 9019 (2002).
[52] C. R. Pidgeon and R. N. Brown, Phys. Rev. **146**, 575 (1966).
[53] J. M. Luttinger and W. Kohn, Phys. Rev. **97**, 869 (1955).
[54] E. O. Kane, *Semiconductors and Semimetals* (Academic, New York, 1966), Vol. 1.
[55] G. L. Bir and G. E. Pikus, *Symmetry and Strain-Induced Effects in Semiconductors* (Wiley, New York, 1974).
[56] I. Vurgaftman and J. R. Meyer, J. Appl. Phys. **89**, 5815 (2001).